Nano Scale Disruptive Silicon-Plasmonic Platform for Chip-to-Chip Interconnection

M40 –Individual plasmonic devices characterization, testing and evaluation

Deliverable no.:	M40.1
Due date:	31/01/2015
Actual Submission date:	11/08/2015
Authors:	TUE/KIT/IMEC/UVEG/UGENT
Work package(s):	WP6
Distribution level:	RE[1] (NAVOLCHI Consortium)
Nature:	document, available online in the restricted area of the NAVOLCHI webpage

List of Partners concerned

Partner number	Partner name	Partner short name	Country	Date enter project	Date exit project
1	Karlsruher Institut für Technologie	KIT	Germany	M1	M36
2	INTERUNIVERSITAIR MICRO-ELECTRONICA CENTRUM VZW	IMEC	Belgium	M1	M36
3	TECHNISCHE UNIVERSITEIT EINDHOVEN	TU/e	Netherlands	M1	M36
4	RESEARCH AND EDUCATION LABORATORY IN INFORMATION TECHNOLOGIES	AIT	Greece	M1	M36
5	UNIVERSITAT DE VALENCIA	UVEG	Spain	M1	M36
6	STMICROELECTRONICS SRL	ST	Italy	M1	M36
7	UNIVERSITEIT GENT	UGent	Belgium	M1	M36

[1] **PU** = Public
PP = Restricted to other programme participants (including the Commission Services)
RE = Restricted to a group specified by the consortium (including the Commission Services)
CO = Confidential, only for members of the consortium (including the Commission Services)

Deliverable Responsible

Organization: Eindhoven University of Technology
Contact Person: Victor Dolores-Calzadilla
Address: Faculty of Electrical Engineering
P.O. Box 513
5600 MB Eindhoven
The Netherlands
Phone: +31 (0) 40247 5129
E-mail: v.calzadilla@tue.nl

Executive Summary

Several plasmonic devices were developed within the framework of the project towards the demonstration of a plasmonic-based chip-to-chip interconnection. Some of such devices have been successfully demonstrated whereas others remain a challenge and are still under development. This report contains the available characterization information of all plasmonic devices.

Change Records

Version	Date	Changes	Author
1 (submission)	2015-08-11		V. Calzadilla, M. Smit

1. Introduction

It is the aim of WP6 to carry out the integration, characterization and testing of the plasmonic devices intended to form the plasmonic interconnection. The devices comprise a nanolaser, a modulator, an amplifier and a detector, from which the last three are based on plasmonic effects.

This report contains the latest characterization information of all individual plasmonic devices. The next section provides a summary of the characterization of all devices. Section three reports the efforts to demonstrate the electrically pumped integrated nanolaser. Then, section four describes the full characterization of the plasmonic modulator, both as a phase modulator and in a Mach-Zehnder configuration. Then, the characterization results of the plasmonic amplifier and photodetector are reported in the fifth and sixth sections, respectively.

2. Summary

We completed the fabrication of the waveguide-coupled metal-cavity nanolaser in a III-V layer stack bonded to silicon. We performed static and dynamic characterization of the devices. The characterization results comprise voltage-current diode curves, light-current curves, spectral characterization, as well as modulation experiments. We tested the devices at room-temperature and cryogenic temperatures. We did not yet observe lasing, but we observed nanoLED operation with on-chip wall-plug efficiency between 10^{-2} and 10^{-4} at 9.5 K and room temperature, respectively, which is well above recent state-of-the-art LED nano-sources. Additionally, we performed correlation measurements (due to the limited optical power) which confirmed that the devices can be directly modulated up to at least 10 GHz of switching speed.

High speed plasmonic-organic hybrid (POH) Mach-Zehnder modulators are demonstrated operating at data rates of up to 40 Gbit/s. We report on on-off keying (OOK) signaling with POH Mach-Zehnder modulators (MZM) at data rates of up to 40 Gbit/s with low energy consumptions of 75 … 225 fJ / bit. In particular, using the 29 µm device we show OOK signaling at data rates of 30 Gbit/s, 35 Gbit/s and 40 Gbit/s with the BERs well below the hard-decision FEC threshold. The measured BERs represent the lowest values, and therefore clearly demonstrating the applicability of plasmonic devices particularly in short-reach optical links. In addition, we demonstrated a latching optical switch that combines the memristor concept with plasmonics. The switch exploits the formation and elimination of a conductive path in the insulating layer of a metal – insulator – metal layer stack. The conductive path leads to an attenuation of the optical mode in the OFF state and is ruptured when switching to the ON state. The plasmonic switch is integrated with a silicon photonic waveguide. Optical extinction ratios of 12 dB at 1550 nm wavelength are shown for 10µm long devices. The operation power is consumed only when the state of the switch is changed and is below 200 nW with operating voltages in the range of 2V and currents below 100 nA. Tests with 50 write cycles and sinusoidal modulation in the megahertz regime demonstrate excellent repeatability of the switching mechanism.

Two concepts of hybrid-plasmonic amplifiers incorporating QDs (using polymer and SiN waveguides) have been fabricated and characterized by using CdSe QDs emitting at visible and HgTe QDs emitting at NIR wavelengths. Metal waveguides (planar and ridges) have been fabricated and used to investigate the observed increase of the SPP propagation length by optical pumping of QDs, even if net gain cannot be achieved by the available material.

In respect to the plasmonic amplifier, two devices were studied: a polymer-based amplifier and a SiN with embedded QDs. We successfully measured the surface plasmon polariton (SPP) propagation length (L_P) in different stripe-like plasmonic waveguides (from 250 to 1000 nm and 10 μm) embedded into a dielectric film (exhibiting photonic modes) containing QDs and confirmed that L_P significantly grows when increasing the pump power. On the other hand, we also developed a platform whereby QDs are embedded in a stack of 2 SiN layers Our preliminary results show possible lasing effect in QD-SiN disk and although detailed measurement at low pump power (below 0.03mW) is needed to confirm whether lasing occurs at a certain threshold pump power.

Regarding the plasmonic photodetector, two kind of structures were investigated. The first one concerns a Schottky-heterostructure photodiode with PbS QDs. In the best generation of devices we have obtained peak responsivities of 0.48 and 0.18 A/W at around 1300 and 1500 nm. In the case of QD-solid based microgap/nanogap photoconductors, for the best device, the 10 μm gap photoconductor, we measured a photocurrent around 40 nA at 1300 nm, which is translated in a responsivity higher than 3 A/W at a bias of 100 V.

3. Metallo-dielectric nanolaser

3.1. Device to characterize

We successfully completed the second fabrication run of devices in a III-V layer stack bonded to silicon. Details of the fabrication are in D3.3 report (“Fabrication of plasmonic laser device”). Figure 1 shows Scanning Electron Microscope (SEM) photographs of the nanodevice before and after metallization.

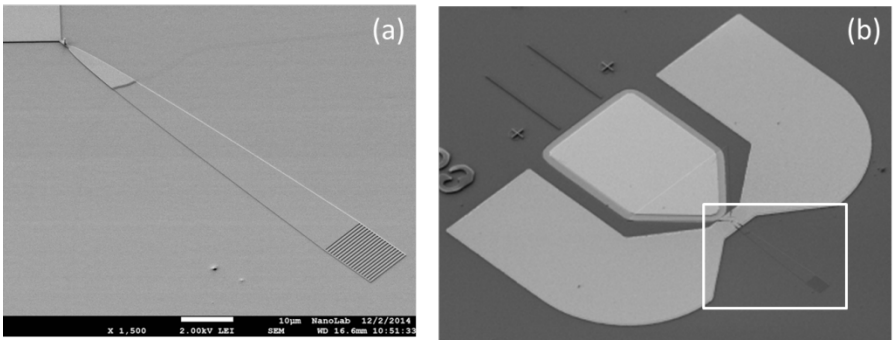

Fig. 1. SEM photographs of the waveguide-coupled nanocavity (a) before metallisation and (b) after metallization. Fig. 1a corresponds to the same are depicted by the white square in Fig. 1b.

Since the cavity resonant wavelength is very sensitive to the cavity size, we fabricated a series of devices with different pillar cross section going from 300x300 nm2 to 360x360nm2, in order to compensate for fabrication inaccuracies.

3.2. Static characterization

We measured the electrical characteristics of the diodes at room temperature and cryogenic temperatures. The electro-optical characterization was done with a micro photoluminescence setup with a helium-cooled cryostat. The devices were electrically contacted with RF probes (ground-signal-ground) and the light emission was collected from the grating coupler with a high numerical aperture lense. The devices showed LED operation and worked both at room-temperature and at cryogenic temperatures.

Figure 2 shows the resonance wavelength for different cavity sizes. Due to the strong confinement of the mode, the resonance wavelength scales linearly with the cavity size.

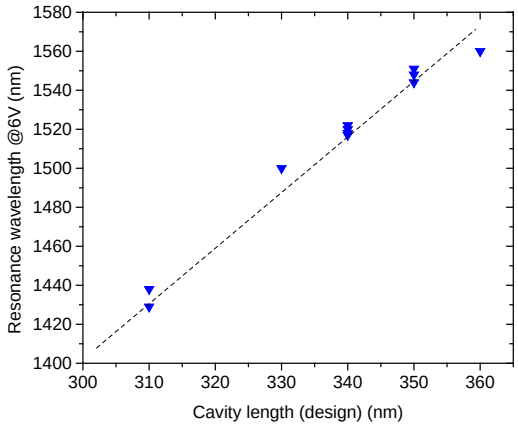

Fig. 2. Resonance wavelength as a function of cavity size for a fixed bias point of 6V.

Representative I-V curves are shown in Fig. 3. As it can be seen, at room temperature the diode hardly shows a turning-on voltage probably due to a high leakage current together with a high contact resistance. Since we did not anneal the p-contact, we expected it to show a high contact resistance. Furthermore, we measured a constant dark current of 0.5µA and 1nA at room temperature and 9K, respectively. We measured a diode resistance of about 30 kΩ in both cases.

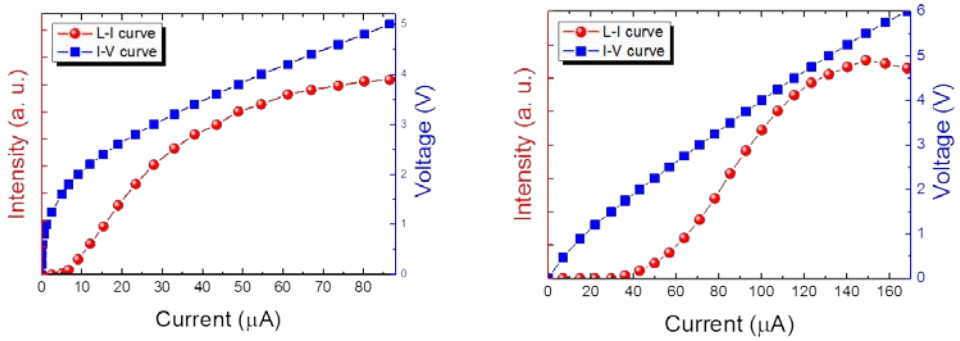

Fig. 3. Current-voltage and light-current curves at 9K(left) and room temperature(right).

Regarding the optical output power, Fig. 3 shows the L-I curves. At room temperature, the optical emission saturates with a current of 140 µA, which corresponds to a current density of 156 kA/cm^2, whereas at low temperature, the emission saturates with a lower injection of about 70 µA.

We observed a high on-chip Wall Plug Efficiency (WPE) between 10^{-2} and 10^{-4} at 9.5 K and room temperature, respectively, as shown in Fig. 4. Such levels of efficiency are remarkably better than recently reported nanoLED and nanolaser devices [1,2], whose efficiencies range between 10^{-5} and 10^{-7}.

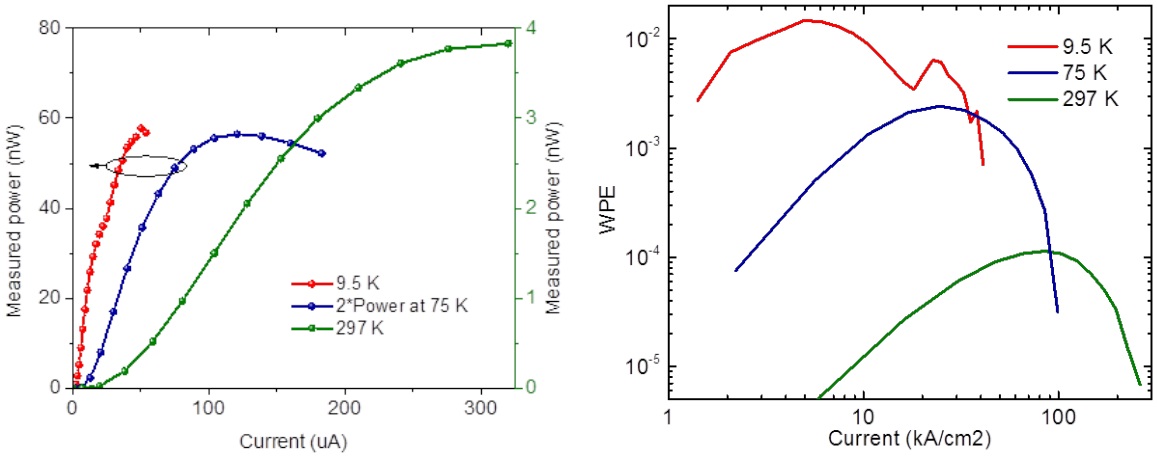

Fig. 4. Left: Light-current characteristics for a device working at 1550nm at different temperatures. Right: On-chip wall–plug efficiency corresponding to the L-I curves shown at the left plus 6 dB to account for grating coupler loss (3 dB) and bi-directional waveguide coupling (3 dB).

Figure 5 depicts the resonance shift of several devices at different temperatures as a function of current injection. As it can be seen, the resonance is initially blue-shifted and later red shifted. Such blue shift is associated with the decrease of the semiconductors refractive index due to carrier injections, whereas the red shift is characteristic of the refractive index change due to temperature increase.

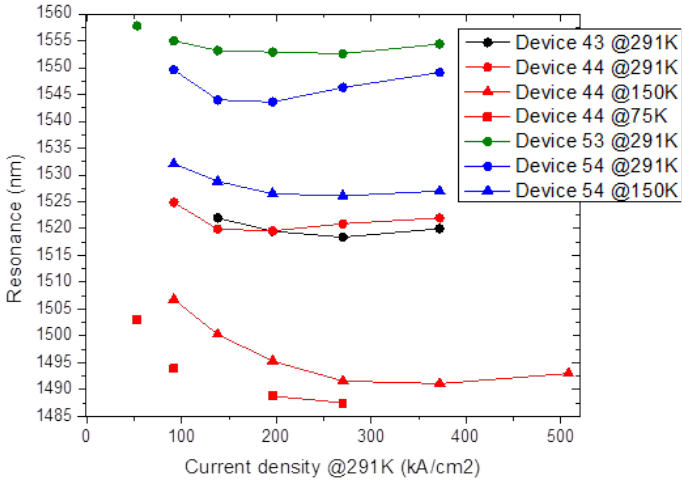

Fig. 5. Resonant wavelength versus current density. The plot shows how the resonance is blue shifted before emission saturation, afterwards red shift dominates.

Figure 6 shows the spectral evolution of the resonance for increasing current injection. As it can be seen, the blue shift is much smaller at room temperature. In Fig. 6(right), only the cavity resonance is visible for very low injection levels, whereas another resonance around 1400 nm shows up for higher current levels. This strong resonance corresponds to a mode bouncing vertically between the top of the pillar and the buffer layer of SiO_2. Overall, we observed a minimum FWHM of 25 nm.

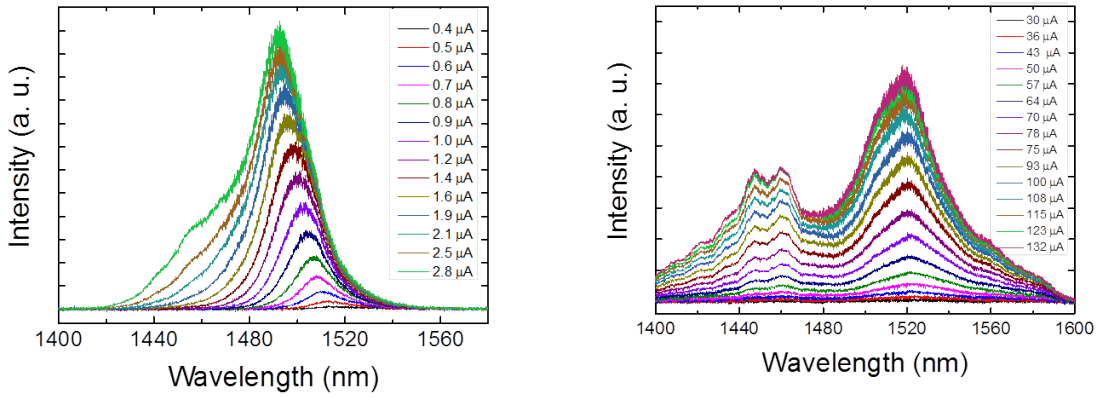

Fig. 6. Spectrum intensity for different current injection at 9K(left) and room temperature(right).

3.3. Dynamic characterization

3.3.1. Description of the experimental setup

In order to measure the dynamic sub-nanosecond response of the nanoLED one performed a time-resolved electrical modulation scheme using the synchronization setup shown in Fig. 7. A probe station setup designed to measure micro-Photoluminescence spectra was employed together with a fast signal pulse generator (Agilent 81134A), a superconducting single photon detector (SSPD) and a correlation card (PicoHarp 300). In this experiment, a high-frequency bias-T (0.2 MHz – 12 000 MHz) was employed to allow to drive the nanoLED samples contacted by high-speed probes with both an a.c signal and a d.c. signal. The voltage generator was employed in pulse mode driving the nanoLED directly with pulse widths as low as 100 ps and repetition rates from 80 MHz up to several GHz. The trigger of the signal generator has been also used as synchronization trigger for the start input of the correlation card. The stop of each experiment is given by the SSPD output. The SSPD input signal corresponds to the filtered PL signal collected with a high numerical aperture objective from the grating output of the nanoLED which is then fibre coupled to a single channel of the SSPD.

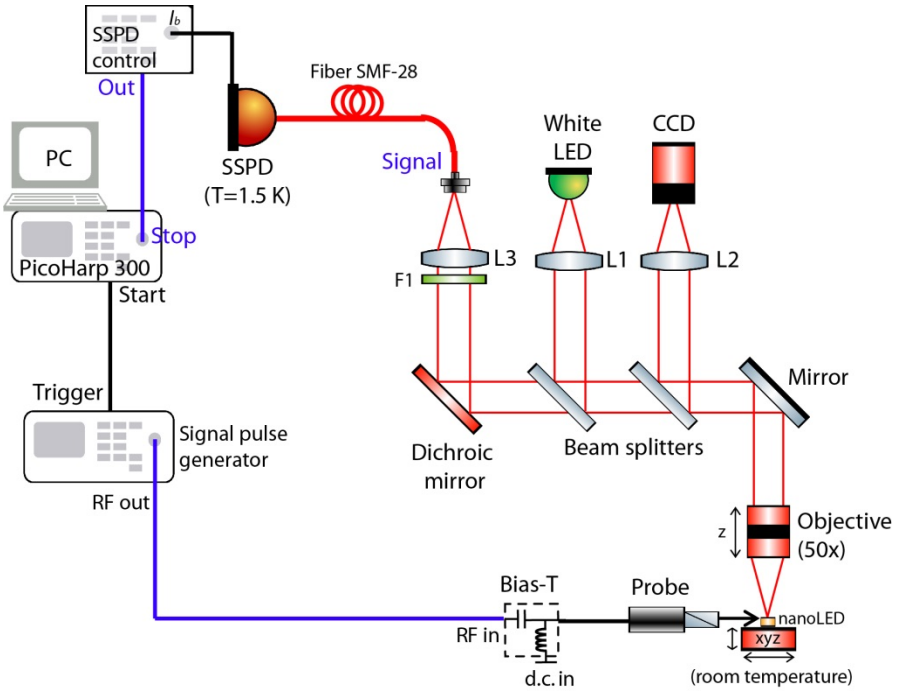

Fig. 7. Experimental setup for electrical modulation of the waveguide-coupled metal cavity nanoLED.

3.3.2. Description of the ultra-fast electro-optical pulse response

Time resolved electro-optical luminescence studies were used to determine the electrical response of our devices. We employed an 80-MHz electrical pulse generator (Agilent 81134A) to drive the nanoLED directly with pulse widths as low as 100 ps. Fig. 8 shows the detected modulated optical ouptut when the nanoLED was d.c. biased with a current of 670 nA (100 mV voltage). The pulse response of the nanoLED is very fast exhibiting a single exponential decay of ~60 ps limited only by the instrument response function of our setup. This result shows that our nanoLED is capable of ultra-fast switching at multiple GHz speed, as shown in the next experiment.

The results in Fig. 8 are compared with the exponential decay of the InGaAs bulk material measured in a sample with an identical epilayer material employed in the fabricated nanoLEDs. The results indicate that minority carrier lifetimes in the nanopillar of the nanoLED are much shorter than the nanosecond-range lifetimes in the bulk material, indicating that the surface states that are a channel of nonradiative recombination are very pronounced. Although the efficiency of our nanoLED can be limited by these non-radiative processes, one can take advantage of the fast recombination processes for attractive applications in fast optoelectronic devices.

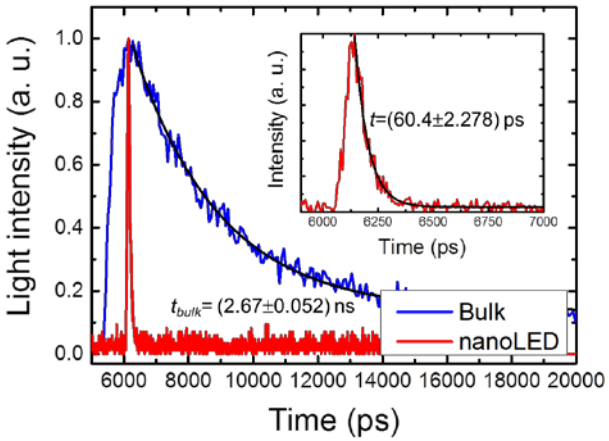

Fig. 8. Time resolved electroluminescence results showing the response of the nanoLED to 100-ps width pulses with 80 MHz repetition rate. The nanoLED was d.c. biased with a current of 670 nA (100 mV voltage). Shown inset is the zoom-in of the nanoLED pulse response exhibiting a single exponential decay of ~60 ps limited only by the instrument response function of our setup. The results are compared with the nanosecond long range exponential decay of the InGaAs bulk material measured in a sample with identical epilayer material employed in the fabricated nanoLEDs.

3.3.3. Description of the Gb/s electro-optical modulation response results

In this experiment, we directly modulated the nanoLED using a pulse pattern generator (Anritsu MP1701A) with a periodic pulse train from 2 GHz to 5 GHz with pulse widths varying from 250 ps to 100 ps, respectively (Fig. 9a). Figure 9b shows the light output showing that the nanoLED replicates well the injected on-off periodic bit sequences. The bit stream has clearly resolvable off-pulses and the on-pulses at 5 GHz are around 100 ps, that is, with identical pulse width of the

injected pulses. These results, although represent a statistical measurement of a time-resolved electroluminescence spectroscopy technique, show promising performance for further tests of these devices in a BER transmission employing high-sensitive avalanche photodiodes able to detect optical signals down to the sub-nanowatt range.

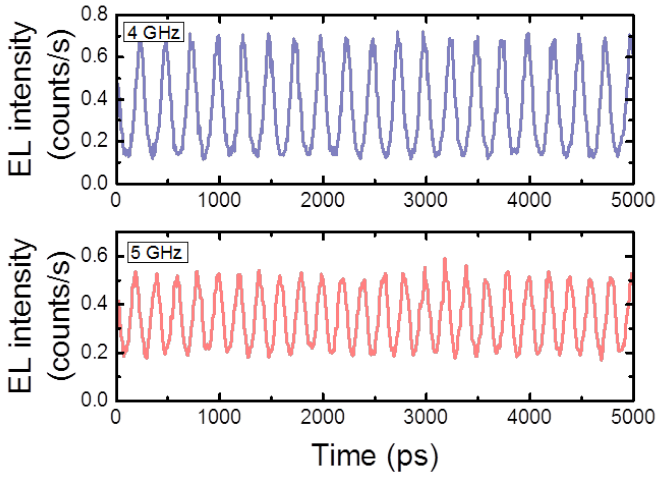

Fig. 9. NanoLED modulation with a pulsed pattern with 50% duty cycle at 4 and 5 GHz (8 and 10 Gb/s NRZ). The devices were driven with a voltage modulation signal of 1.44 V peak-to-peak amplitude.

3.4. Conclusions

We reported the characterization of waveguide-coupled nanoLEDs. We fabricated the devices in an InP-membrane on silicon photonic platform. The devices worked at cryogenic and room temperature over a wavelength range of 1400 nm to 1550nm, and were characterized through grating couplers.

We observed LED operation with a maximum optical power of 60 nW, minimum FWHM of 25 nm, an on-chip wall plug efficiency ranging from 10^{-4} to 10^{-2} depending on the temperature. We also carried out statistical modulation experiments to investigate the dynamic characteristics of the devices. We demonstrate the nanoLED device exhibits sub-100 picosecond response to electrically injected short pulses and up to 5 GHz (10 Gb/s NRZ) electro-optical modulation. The results are limited only by the instrument response function of our setup and modulation speeds of our signal pulse generators meaning that faster modulation speeds are possible.

Dedicated experiments in our laboratory revealed that the devices suffered from strong surface recombination, which contributed to prevent lasing. Although lasing was not reached due to cavity losses higher than expected, their realization represents a significant progress for on-chip efficient and fast nano-light sources in integrated photonics.

References

[1] Kevin C. Y. Huang et al., "Electrically driven subwavelength optical nanocircuits", Nature Photonics 8, 2014.
[2] Bryan Ellis et al., "Ultralow-threshold electrically pumped quantum-dot photonic-crystal Nanocavity laser", Nature Photonics 5, 2011.

4. Plasmonic modulator

4.1. Plasmonic absorption modulator

The plasmonic absorption modulator as described in deliverable 3.4 was characterized in two steps. First, we studied the quasi-static behavior. We measured the current and the optical transmission while slowly sweeping the applied voltage. In a second step, a MHz modulation was applied to the device. In summary, the device shows optical extinction ratios of 12 dB at 1550 nm wavelength for 10 µm long devices. The operation power is below 200 nW with operating voltages in the range of ±2 V and currents below 100 nA. Tests with 50 write cycles and sinusoidal modulation in the MHz regime demonstrate excellent repeatability of the switching mechanism.

4.1.1. Static behavior

We measured the current and the optical transmission as a function of the applied voltage. The voltage was applied between top and bottom electrode. A compliance current of 100 nA was set to protect the device from permanent breakdown. Continuous wave laser light at a wavelength of 1550 nm was coupled to the chip through grating couplers. The transmitted optical signal was measured with a power meter.

The electrical behavior of a 5 µm long device with the laser being turned off is displayed in Fig. 10. The applied voltage was swept from -3 V to 3 V and back in steps of 60 mV with a duration of 2 s per step. We observed a sudden increase of the current at a threshold of ~2.9 V. Here, the current reached its compliance limit. When scanning back, the current decreased while showing a hysteresis.

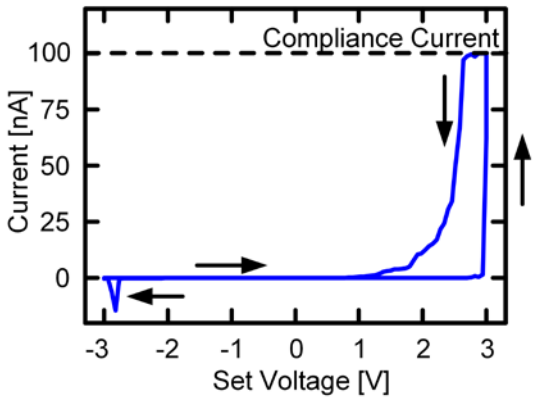

Fig. 10. Electrical current-voltage characteristic of the plasmonic absorption modulator. The response indicates a hysteresis. An abrupt increase of the current is found with a threshold around 2.9 V. Note that the set voltage differs from the actual (measured) voltage in the compliance limit.

Fig. 11(a) shows the normalized optical transmission for 50 consecutive measurement cycles below threshold (±2 V, 20 mV per step, 2 s per step, total duration of 13.3 min per cycle). We started at -2 V in the ON state. While gradually increasing the voltage, the optical signal decreased. When decreasing the voltage, the optical transmission increased again, while being lower than for the forward sweep direction. This hysteresis indicates a memory effect of the switch. The device returned to its initial state after completion of each measurement cycle. This shows excellent repeatability of the switching effect. The difference between the ON and the OFF state (extinction ratio) was 6 dB. The latching extinction ratio between the latched states was 3.5 dB. Since the device was operated below threshold, no significant current was measured and no hysteresis was observed in the I-V curve. Therefore, peak operating power during switching is below 200 nW.

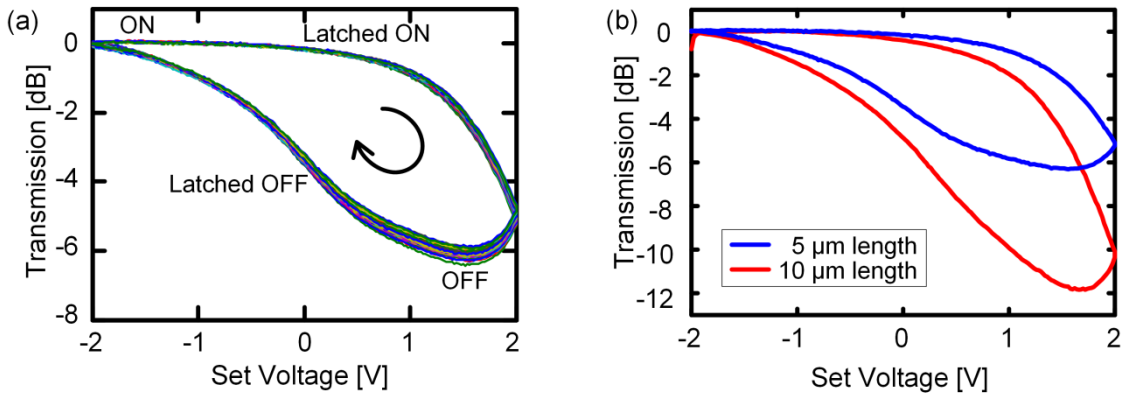

Fig. 11. Quasi-static performance of the plasmonic absorption modulator. (a) Latching optical switch behavior for a 5 µm long device: 50 measurement cycles of the normalized optical transmission as a function of the set voltage showing a hysteresis and an extinction ratio of 6 dB. (b) Latching optical switch behavior of a 10 µm long device showing an extinction ratio of 12 dB. During these measurements below threshold, no hysteresis was observed in the I-V curve.

The dependence of the extinction ratio on the device length was investigated as well. From Fig. 11(b) one can see that increasing the length from 5 µm to 10 µm increases the extinction ratio from 6 dB to 12 dB. Thus, the extinction ratio increases with increasing device length. While two devices with different lengths do not yet provide sufficient statistics the result at least indicates a trend.
Propagation losses in the hybrid waveguide section of 1 dB/µm and coupling losses between the silicon photonic and the hybrid waveguide of 6.5 dB per interface were determined through cut-back measurements.

4.1.2. Dynamic behavior

To further assess the device, we studied the dynamic behavior of the switch. Here, a sinusoidal modulation in the MHz regime was applied to the device and detected with a photodiode and a lock-in amplifier. This revealed a relatively flat frequency response between 40 kHz and 10 MHz. The 3 dB bandwidth at an operation with ± 2 V with respect the amplitude at 40 kHz is 30 MHz (see Fig. 12, blue triangles).

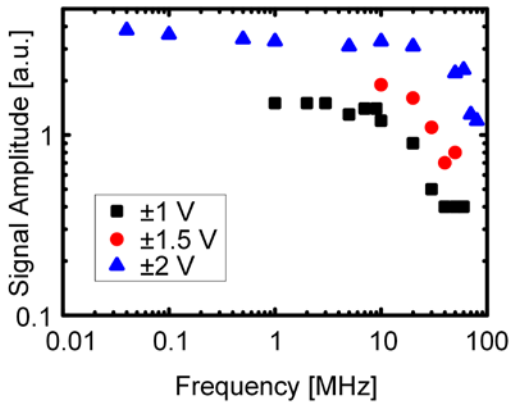

Fig. 12. MHz frequency response of the plasmonic absorption modulator. A sinusoidal signal was applied to a 5 µm long device using an arbitrary waveform generator. The optical signal was detected with a photodiode and a lock-in amplifier.

4.2. Plasmonic Mach-Zehnder modulators

The plasmonic Mach-Zehnder modulator consists of two high speed plasmonic phase shifters (see Fig. 13(a), Deliverable 3.2 and Deliverable 3.4) placed in the arms of a Mach-Zehnder interferometer realized on a silicon-on-insulator (SOI) wafer. The interferometer is designed with un-balanced arms and the operation point of the modulator is defined by the operating wavelength, see Fig. 13(b). Standard photonic multimode interference (MMI) couplers have been used as 3dB optical splitters/combiners. High speed phase modulation is performed by plasmonic phase shifters based on the Pockels effect in an electro-optic (EO) organic material,

see Fig. 13(a). Applying a voltage between the metal electrodes can change the refractive index of the EO-material due to the Pockels effect, and therefore the phase velocity of the plasmonic mode. The photonic-to-plasmonic mode conversion within the arms of the Mach-Zehnder interferometer is accomplished by the metal taper couplers. Scanning electron microscope image of the active plasmonic phase shifter section is give in Fig. 13(c) and Fig. 14(a)-(c). To keep the insertion loss of the modulators in the practical range we use low loss silicon MMI with an insertion loss of less than 0.5dB.

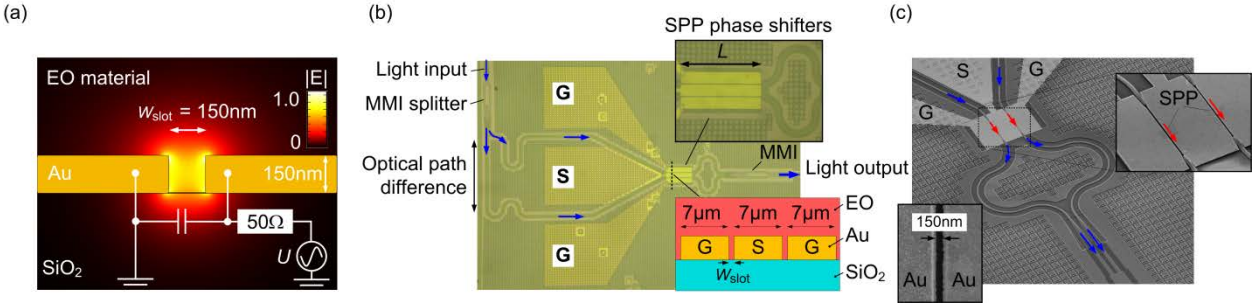

Fig. 13. Silicon-plasmonic Mach-Zehnder modulator (MZM) designed and fabricated on a silicon-on-insulator (SOI) platform. (a) Gap surface plasmon polariton (SPP) mode profile in a metal slot filled with an electro-optic (EO) material. The SPP mode is strongly confined to the slot. In addition, a lumped-element equivalent circuit of the modulator is given. Because of the high conductivity of the gold electrodes, the device can be represented by a capacitor ($C_{Device} \approx 1.5...3$ fF, L dependent). (b) Optical microscope image of the fabricated Mach-Zehnder (MZ) modulator. The MZ interferometer is defined on a passive silicon platform, where light splitting / combing is done by low loss photonic multimode interference (MMI) couplers. The photonic to plasmonic mode conversion is accomplished by metal taper couplers. An optical path difference is implemented in the MZ interferometer design to avoid applying high bias voltages. An optical phase difference between the two arms is modulated by the plasmonic phase shifters. (c) Scanning electron microscope (SEM) picture of the silicon-plasmonic MZM. The modes of the silicon waveguide are coupled to the plasmonic phase shifters, where the phases of the SPPs are modulated. In the end of the phase shifters the SPPs are back converted to photonic modes and then combined within the photonic MMI coupler

The Mach-Zehnder modulators are fabricated on a silicon-on-insulator (SOI) platform with a buried oxide with a thickness of 2mm, and a silicon device layer with a thickness of 220 nm. First, the passive silicon photonic circuit is fabricated at IMEC, in the frame work of ePIXfab, by using standard processes such as 193 nm DUV lithography and Si dry etching. The plasmonic high-speed phase shifters with a common signal electrode are defined on gold (Au). The metallic slots with the widths of ~150 nm slot and the length of 19 µm, 29 µm and 39 µm are defined with e-beam lithography and lift-off process. The slot is filled with an electrooptic material SEO100 (Soluxra, LLC). The electro-optic effect in the EO material is activated through a poling procedure. To avoid electrical breakthroughs, we perform the poling with electrical fields which are lower than the optimum poling field of 100 V/µm corresponding to the maximum r_{33} = 110pm/V.

4.2.1. Characterization results of the photonic-to-plasmonic mode converters

We first characterize the photonic-to-plasmonic mode converters using the fabricated test samples consisting of single metallic slot waveguides interfacing to silicon nanowires through

two metallic taper mode converts, see Fig. 14(a) – (c). By varying the length L_{MSW} of the metallic slot waveguide between the pairs of taper couplers we can extract the conversion efficiency similar to the standard cut-back measurement. Three devices with metallic slot waveguide lengths of L_{MSW} of 1 mm, 29 mm, and 44 mm, see Fig. 14(a) – (c). The slot width is about 140 nm for all three cases.

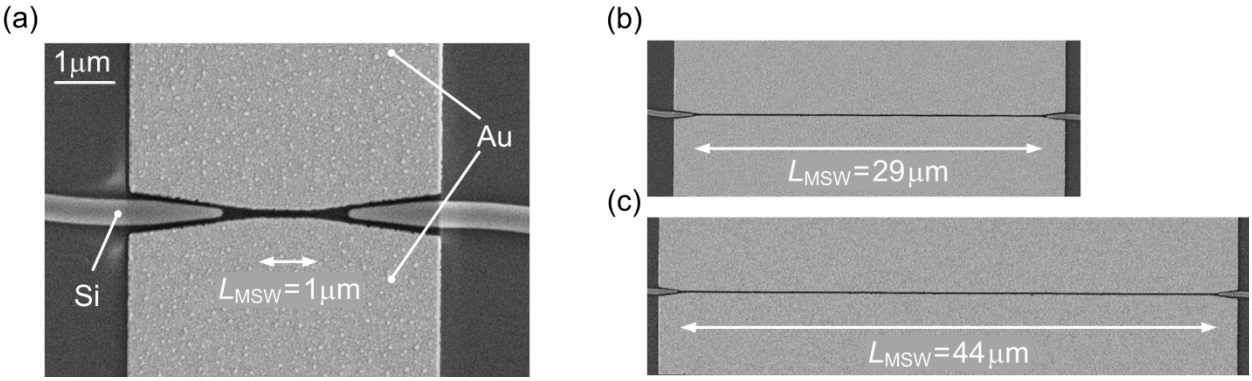

Fig. 14. Fabricated metallic tapered mode converters with three different MSW lengths LMSW of (a) 1 mm, (b) 29 mm, and (c) 44 mm. The slot size h is about 140 nm for all three devices.

The measured silicon-to-silicon waveguide transmission spectra for the three different metallic slot waveguide lengths L_{MSW} are given in Fig. 15(a). The measured transmission spectra are normalized to the measured reference spectra for a silicon strip waveguide without a plasmonic section. As can be seen, the tapered mode converters exhibit large conversion efficiency in a wide operating wavelength range. A total conversion loss of 1 dB is estimated for two transitions. This is in agreement with the theoretically expected conversion efficiency of 2…3 dB. The difference between theoretically calculated and experimentally measured conversion efficiencies is attributed to small differences of the fabricated slot widths and variations of the sidewall roughness of the metallic slots.

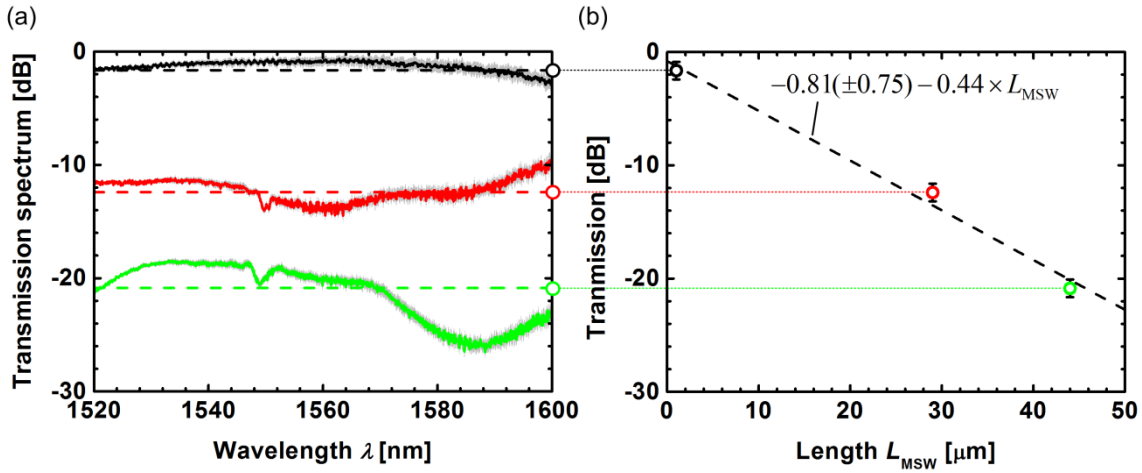

Fig. 15. Fabricated metallic tapered mode converters with three different MSW lengths LMSW of (a) 1 mm, (b) 29 mm, and (c) 44 mm. The slot size h is about 140 nm for all three devices.

4.2.2. Static behaviour of plasmonic Mach-Zehnder modulators

Power transmission spectra for all three MZMs are given in Fig. 16(a). In addition, the transmission spectrum of a reference Mach-Zehnder interferometer is given without a plasmonic phase shifter. It can be seen that, that silicon grating couplers have a big contribution in the total insertion loss of our silicon-plasmonic Mach-Zehnder modulators. With the state of the art fiber to silicon-waveguide couplers with 1dB loss the total insertion loss of the current silicon-plasmonic Mach-Zehnder modulators can be reduced down to 13-20 dB depending on the length of the plasmonic phase shifters. The extinction ratio and the free spectral range (FSR) vary among the devices because of the uncertainty in defining the width and quality of the metallic slots. The shift of the wavelength corresponding to the minimum transmission with the applied voltage is measured in order to estimate the voltage U_p required for having a phase shift of p. An example of the transmission spectra for voltage off and on states are given in Fig. 16(b) for the MZM with the 39 µm long phase shifters. Measuring the wavelength shift Dl_0 for the applied voltage of U_0, we calculating $U_p = Dl_{FSR} \times U_0 / (2Dl_0) \approx 30$ V for MZM with 39 µm long phase shifters and that the $U_p = 37$ V for the MZM with the 29 µm long phase shifter.. In particularly, we achieve on-chip electro-optic coefficient r_{33} in the range of 70 pm/V. This value is significantly lower than the maximum value of 110 pm/V specified for bulk. These values can further be improved by optimizing the poling procedure of the EO material and improving the fabrication of the metallic slots.

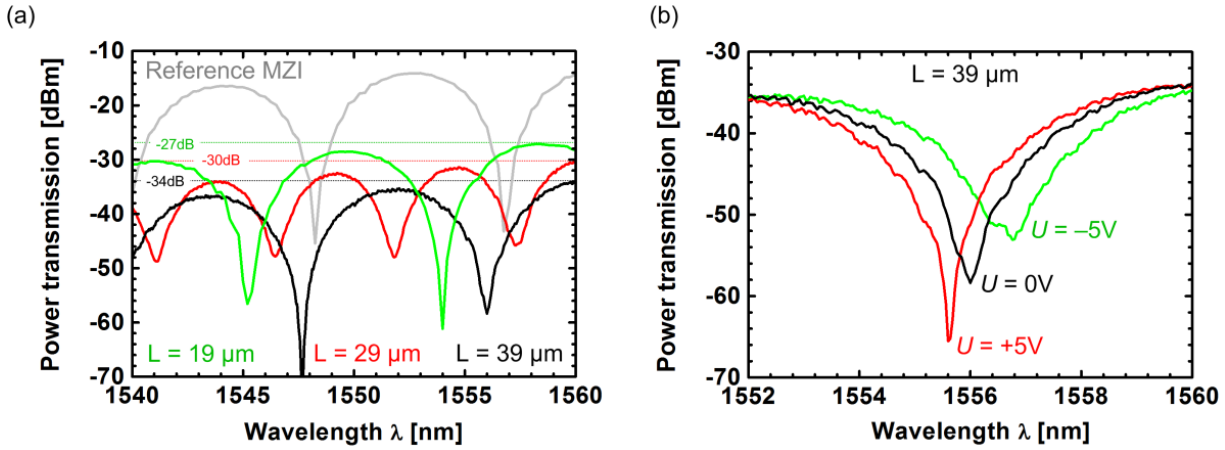

Fig. 16. Static characterization results for the Mach-Zehnder modulators. (a) Fiber-to-fiber power transmission is given for the MZMs with the length of 19 µm, 29 µm and 39 µm. In addition, we give the transmission spectrum of a reference Mach-Zehnder interferometer without a plasmonic phase shifters. The plasmonic phase shifters add 13 dB to 20 dB additional optical loss. (b) Transmission spectrum of the 39 µm long device is given for various applied voltages. Analyzing the shift of the wavelength corresponding to the minimum transmission we estimate the voltage U_p required for having a phase shift of p.

4.2.3. Data modulation

Next, data modulation experiments have been performed with the plasmonic MZM using a direct receiver setup as shown in Fig. 17(a). An electrical non-return-to-zero (NRZ) signal with PRBS pattern length of 2^{31}-1 and with a peak-to-peak voltage swing of 5 V (measured across a 50 W resistor) is fed to the modulator via a ground-signal-ground (GSG) RF probe. The operating point for the MZM is defined by selecting the operating wavelength. The MZMs are operated in the quadrature points, i.e., the modulator output intensity changes linearly with the relative phase difference of the two arms. The OOK signal after the MZM is detected with a standard pre-amplified direct receiver comprising a single erbium doped fiber amplifier, an optical band-pass filter with a bandwidth of 2 nm, a bit-error-ratio tester (BERT), and a digital communication analyzer (DCA).

We measured the BERs for all three MZMs at a bit rate of 30 Gbit/s in order to find the optimum length for the phase modulators. During the experiment, the EDFA of the receiver is operated in constant output power mode. The input optical power to the modulator is varied from +10 dBm to +23 dBm. This varies the input power to the receiver, i.e., the optical signal-to-noise power ratio (OSNR) at the photodiodes. The optimum length of the PS is defined by a compromise between insertion loss and modulation index — making the device too short results in small optical modulation amplitude, while a too long phase modulator section decreases the receiver's input power. We find that in our case (U_{pp} = 5 V, SPP propagation losses of ~0.4 dB / µm, r_{33} = 70 pm/V) the optimum performance can be achieved with 29 µm long phase modulators, see Fig. 17(b). A better BER can be achieved by either increasing the optimum PM length L by improving the slot quality (decreasing optical losses), or by reducing the effective PM length by increasing the electro-optical coefficient and reducing the slot (increasing the optical modulation amplitude). The eye diagrams measured after the MZM with 29 µm long PM sections for bit rates of 30 Gbit/s (BER = 2×10^{-5}), 35 Gbit/s (BER = 3×10^{-5}) and 40 Gbit/s (BER = 6×10^{-4}) are given in Fig. 17(c). These BER are well below the threshold of 4.5×10^{-3} for hard-decision FEC codes with 7% overhead. The driving voltages and the optical insertion losses can be further reduced by, first, optimizing the poling procedure and thereby achieving higher electro-optic coefficients, second, reducing the slot size, and third, by using silver instead of gold.

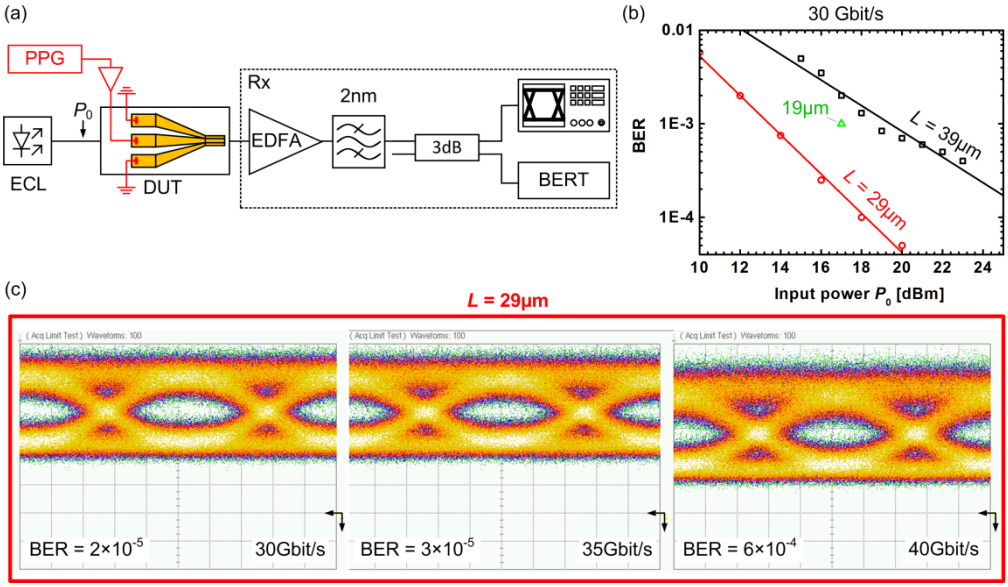

Fig. 17. Modulation experiments with plasmonic silicon-organic MZMs with PM lengths of 19 µm, 29 µm and 39 µm. (a) Direct receiver setup used for detecting on-off keyed signal after the plasmonic MZMs. (b) Bit error ratios measured for the MZMs with plasmonic phase modulator sections having lengths of 19 µm, 29 µm and 39 µm. To find the optimum phase shifter length, we vary the input power to the modulators and measure the BER. A comprise between the optical loss and the modulation index can be achieved by using a MZM with a PM length of 29 µm. (c) Eye diagrams measured at bit rates of 30 Gbit/s (BER = 2×10^{-5}), 35 Gbit/s (BER = 3×10^{-5}) and 40 Gbit/s (BER = 6×10^{-4}) for a MZM with 29 µm long PM sections at an input optical power of 20 dBm and at an operating wavelength of 1556.8 nm. The difference in the DC levels for data rates of 35 Gbit/s and 40 Gbit/s is attributed to the thermal drift of the operating point as a consequence of the large optical input power.

5. Plasmonic amplifier

5.1. Polymer based version (UPDATED 28-7-2015)

We have studied plasmonic structures through a direct measure of the propagation length (L_p) of the surface plasmon polariton (SPP) modes propagating on stripe-like plasmonic waveguides and the effect of QDs-layers on L_p. The method consists in measuring the spatial decay of the TM mode (the long range SPP) from the sample edge by coupling the QD photoluminescence (PL) light (600 nm) that is excited by a probe fiber tip, as measured by the method illustrated in Fig. 18a. In a second step we studied the possible enhancement of the L_p when the QD-nanocomposite is optically pumped. For this purpose a pump laser beam (450 nm) was coupled in the structure along the dielectric planar waveguides integrated on the left and on the right of the Au stripe, as shown in Figure WP4-26b. In order to separate the PL signal used in the probe from that of the pump we have modulated the probe at a frequency around 1 kHz and measured the influence of the optical pumping of the QD-nanocomposite on that modulated signal (using a lock-in amplifier).

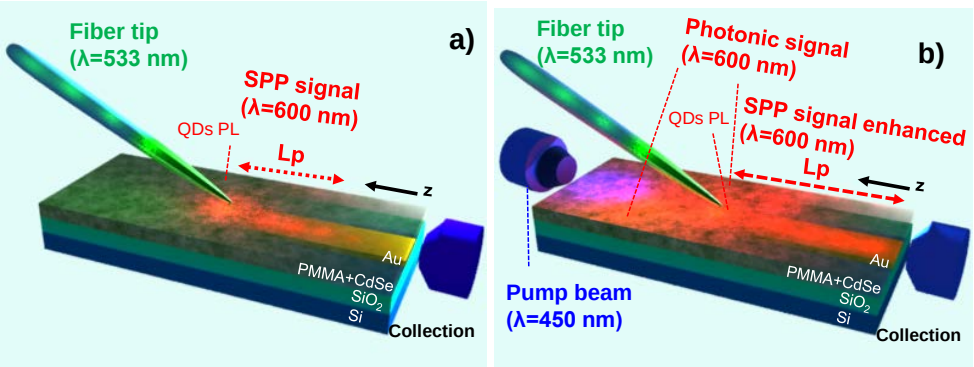

Fig. 18. a) SPP excitation with a fiber tip. The tip provides a small spot on the sample at a wavelength (533 nm) smaller than the QD band-gap (600 nm). Then the PL is coupled to the waveguide modes (LR-SPP mainly) and the L_P of the modes is characterized by measuring the intensity as a function of the distance between the tip and the edge of the sample. b) Loss compensation by coupling a pump beam (450 nm) at the input edge of the sample. This light can propagate through the dielectric waveguides outside the stripe and excite light emission from QDs.

The above described method was satisfactorily used to measure L_P of the propagating long range SPP in different stripe-like plasmonic waveguides (from 250 to 1000 nm and 10 μm) embedded into a dielectric film (exhibiting photonic modes) containing QDs, whose PL signal (CdSe QDs emitting at 600 nm was used as test material) is excited by the fiber probe tip (Fig. 18a). Figure 19a compares measured values (data symbols with error bars) and calculated curve (red continuous line) for L_P, where we observe a clear increase from 10-17 to 50-70 μm, when reducing the stripe width down to 250 nm.

When a 450 nm pump beam is end-fire coupled along the dielectric waveguides containing the QDs, L_P significantly grows by increasing the pump power (PL produced in the QD-nanocomposite), as summarized in Fig. 19b. In fact, the value of L_P of the long range SPP increases from 40 μm to more than 1 mm (25 times enhancement) when using a laser pumping power of 20 mW, in the case of the 250 nm wide Au-stripe, in comparison to the case of the 1000 nm wide Au-stripe where *Lp* increases from 11 μm to 400 μm (≈ 35 times enhancement), as observed in Figure 19b. This experimental behaviour was also corroborated by simulations of light propagation along the Au-stripe with an active three dimensional beam propagation method incorporating light generation without (probe) and with optical pumping (+probe); clearly, the optical pumping of the QD-nanocomposite significantly improves the light coupled into the stripe, evidently with the same phase as the SPP directly generated by the probe that is being modulated.

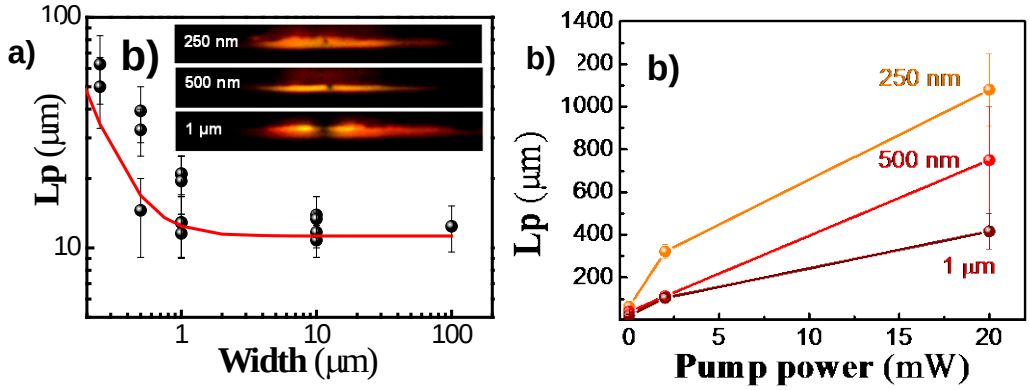

Fig. 19. a) L_P of the LR-SPP mode measured (data symbols) and calculated (red continuous line) in waveguides whose width varies from 250 nm to 100 µm (planar waveguide). Calculations were made by using an effective refractive index method. The inset corresponds to images of the waveguided signal in TM polarization at the output of 250, 500 and 1000 nm wide Au-stripes. b) L_P as a function of the pump power for 1 µm, 500 nm and 250 nm wide Au-stripes.

HgTe QD material was also used to corroborate the enhancement of L_P in plasmonic waveguides at infrared wavelengths, even if in this range we have the limitation of a worse signal-to-noise ratio (by the use of an InGaAs photodiode array instead of a Si CCD). Plasmonic planar waveguides were cladded by PMMA and the HgTe-PMMA nanocomposite; in tis case the symmetry of the refractive index above/below the gold layer is broken and the long range SPP is not supported. The TM signal has a clearly different intensity distribution and a larger attenuation as compared to that of TE (Fig. 20a). The dependence of the guided TM-light as a function of the distance tip-edge exhibits a double exponential decay (black symbols in Fig. 20b), characterized by $L_P(1) \approx 18$ µm, associated to the short range SPP, and $L_P(2) \approx 67$ µm that we attribute to an hybrid photonic-plasmonic mode (see D4.4). After coupling a pump beam to the input edge of the sample, the estimated value L_P for both modes is enhanced by a 15 % (red curve of Fig. 20b). Further experiments are planned for next September with new HgTe QD material and using sub-micrometric Au-stripe waveguides.

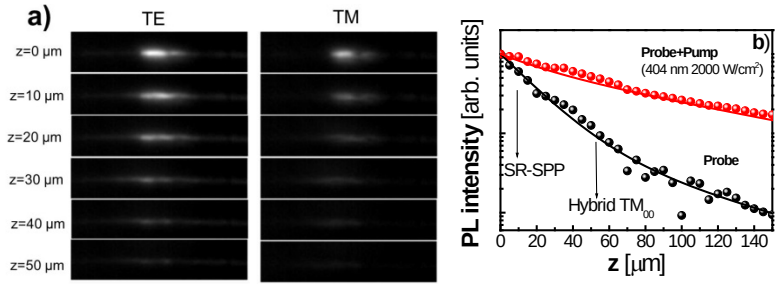

Fig. 20. Near field images (a) and detected signal as a function of the fiber tip to edge distance at 1.55 µm without (black) / with (red) optical pumping of QDs (b) in the sample described in the text (*ff* = 0.08).

5.2. SiN with embedded QDs (UPDATED 28-7-2015)

As discussed in WP4, next to the polymer based platform, we also developed a platform whereby QDs are embedded in a stack of 2 SiN layers. Below we summarize the most important results. Figure 21 shows results for a SiN-QD microdisk device, pumped with different intensities. We herebey used ~55nm thick CdSe/CdS core/shell QDs. To carry out the PL characterization, we used a focused beam (spot size ~100μm diameter) to pump the disk from the top and collected PL from the cleaved facet of the access waveguide using microlensed fibers. We pumped with two different laser beams denoted MAITAI and TOPAS. "MAITAI" is a 80 MHz femtosecond Ti:Sapphire laser at 400nm wavelength, and "TOPAS" is 1 kHz amplified system with higher pulse energy at 450nm. We observed clearly that spontaneous emission of QDs is coupled to the whispering gallery modes (WGM) of the disk and the background PL signal is quite small, since the location of QDs are perfectly aligned with the maximum of the light field in the disk, resulting in an efficient coupling of the QD emission into the disk modes. Note that the envelope of the PL spectrum for the MAITAI arises from the wavelength-dependent spontaneous emission of the QDs. When pumping with the higher power TOPAS, the PL spectrum shows significantly different features compared to the pumping with MAITAI. The narrowed-down spectral envelope (~10nm width) is clearly observed and only a few of the WGM modes remain. This narrowed-down spectrum might be from the ASE of QDs.

In the right picture we show the PL spectra of a disk of 15 μm diameter pumped with different power of TOPAS. Again we observe the narrowing feature of the spectra similar to the 20 μm diameter disk shown on the left. On the other hand, the intensity of the spectra shows evident sensitivity to the pump power and it increases rapidly from 0.02 to 0.03mW pump power while it decreases when further increasing the pump power to 0.15mW. If we plot the integrated PL intensity as a function of pump power it is very clear that the overall output PL power gains sharply and then decays gradually as strengthening the pump power. This preliminary results show possible lasing effect in QD-SiN disk and detailed measurement at low pump power (below 0.03mW) is needed to confirm whether lasing occurs at a certain threshold pump power. At higher pump power region a saturation output power is expected while a reduction of PL is actually observed. This could be attributed to heating effect of the disk when increasing the pump power; however it still needs to be investigated.

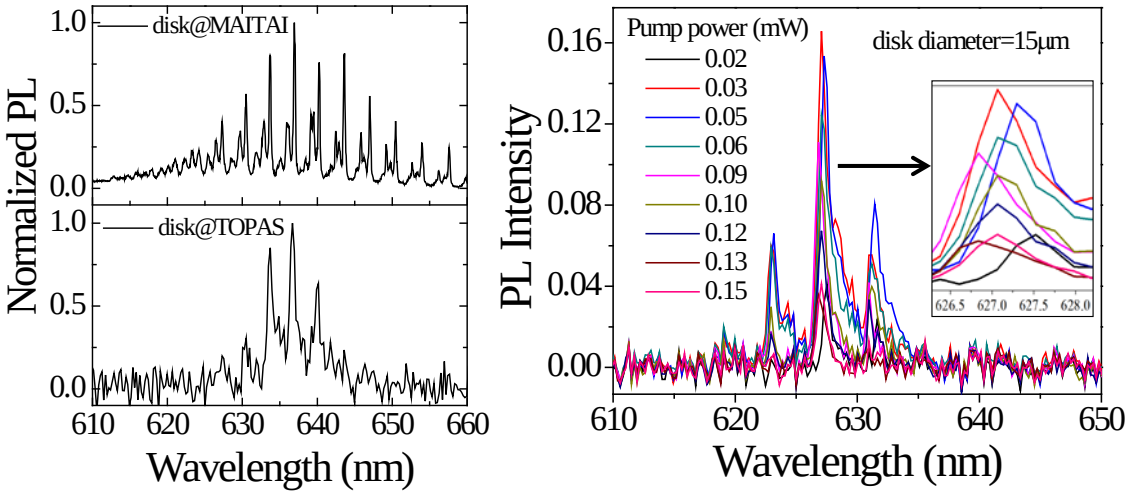

Fig. 21. (a) PL spectra under different pump power of TOPAS. (b) Integrated PL intensity as a function of pump power.

Next to the disk based devices we also characterised straight waveguides with embedded QDs. The figure below shows the pumping scheme (using a cylindrical lens focussing the light to a 10um stripe) and the output power as function of the pump power. Also in this case clearly spectral narrowing and non-linear increase of the output power was observed under pumping ("TOPAS")(followed by saturation at high pump powers). See MS24 for more details.

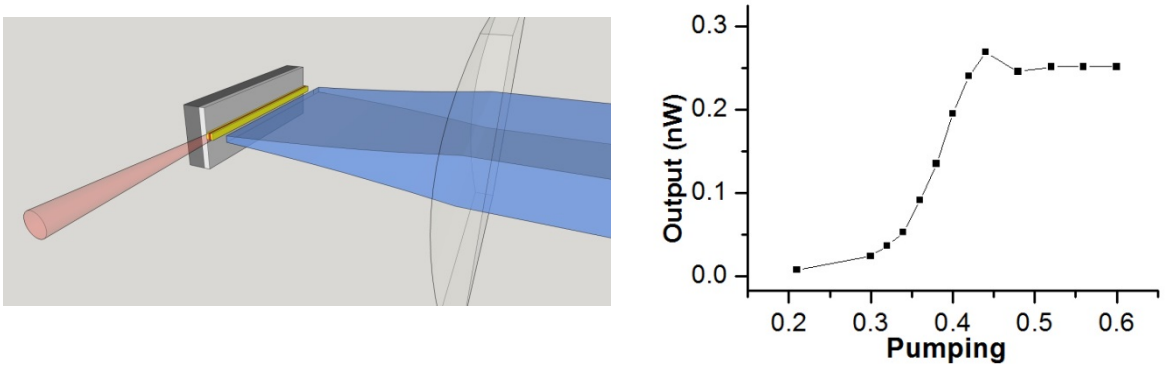

Figu. 22. a) Pump configuration and b) output power as function of pump power for SiN-amplfiers with embedded QDs.

6. Plasmonic photodetector

6.1. Schottky-heterostructure photodiodes

We have optimized the synthesis of PbS QDs with absorption/emission at wavelengths around 1550 nm, as also the deposition (+ ligand exchange) of thin films in the thickness range 300-500

nm by means of a Dr.Blading technique. These layers exhibit a reasonable uniformity throughout the sample, as revealed by exciton absorption and photoluminescence (PL) spectra very close to those in colloidal solution. Layers with completed ligand exchange have a resistivity around 10^5 Ωcm, a hole concentration larger than 10^{15} cm^{-3} and mobilities smaller than 0.065 cm^2/Vs, as estimated from preliminary Hall measurements. These Schotky diodes have been characterized under laser illumination at 1550 nm as a function of power (Fig. 23a-b). The I(V) characteristics can be fitted by using a real equivalent circuit for the photodiode that yields a dark current around 70 nA with an ideality factor around 3 (carrier generation-recombination mechanism) and shunt resistance (attributed to hole losses through the Ag electrode) decreasing with increasing illumination. The photocurrent increases practically linear (exponent = 0.92) with power from 6 nW (I_{cc} = 0.8 nA, V_{oc} = 9 mV) to 2 µW (I_{cc} = 190 nA, V_{oc} = 70 mV), as shown in Fig. 23b, and R ≈ 0.1 A/W in the entire range. In the best generation of devices we have obtained peak responsivities of 0.48 and 0.18 A/W at around 1300 and 1500 nm (blue and green lines in Figure 23c), respectively, even if the ground state exciton absorption was outside our spectrometer range, i.e., beyond 1650 nm. The time response of these photodiodes working in photocurrent mode is estimated to be around 100 □s, very similar to values reported in literature. The photovoltage noise was measured to be of the order of 85 $nV/Hz^{1/2}$ at 1 kHz for the photodiode based in the 500 nm thick PbS QD film, whereas the photocurrent was perfectly linear over more than three orders of magnitude (constant responsivity), with an estimated experimental detectivity in the range of 10^{12} - 10^{13} Jones.

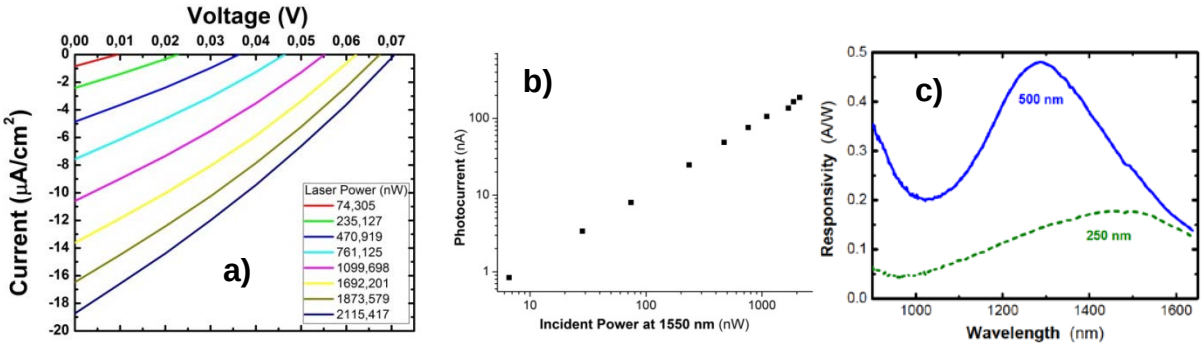

Fig. 23. (a) I(V) characteristics of the best ITO/PDOT/PbS-QD-solid/Ag photodiode (at 1550 nm) under illumination with a laser at 1550 nm at different powers; (b) power dependence of the measured photocurrent (from a); (c) Responsivity measured in the best fabricated photodiodes using the same PbS QDs to deposit 250 (green dashed line) and 500 nm (blue continuous line) thick films.

6.2. QD-solid based microgap/nanogap photoconductors

The Schottky concept is a very convenient device to be integrated in SOI technology, because photocurrent or photovoltage can be directly measured without needing of polarization or used as input for a transimpedance amplifier. However, microgap and nanogap photoconductive devices would offer the most ideal geometry to be integrated in a planar geometry of the final plasmonic chip targeted in NAVOLCHI, other than smaller footprints and adding plasmonic effects in the case of the nanogap photoconductor.

In the case of single microgap and interdigitated photoconductors the electrodes are patterned on the Si/SiO_2 wafer and created by using lift-off processing. For this reason, contrary to the case of Schottky photodiodes, the QD-solid films should be created in a subsequent step by dropping the QD solution, previous to the ligand exchange procedure and curing. This method is not ideal, because the weak control of the QD-solid thickness and the formation of important granularity. For the best device, the 10 μm gap photoconductor, we measured a photocurrent around 40 nA at 1300 nm (Fig. 25a), which is translated in a responsivity higher than 3 A/W at a bias of 100 V. It is important to mention that microgap devices degrade faster with exposure to ambient conditions, specially humidity, than Schottky photodiodes, possibly due to the protecting effect in the latter case by the top Ag-electrode. For this reason an encapsulation of photoconductor devices will be needed after the final ligand exchange and curing processing. Finally, it is important to note that microgap photoconductors have a more important responsivity for lower incident powers, as shown in Fig. 25b, decreasing by more than one order of magnitude from 100 nW to 100 μW of incident power.

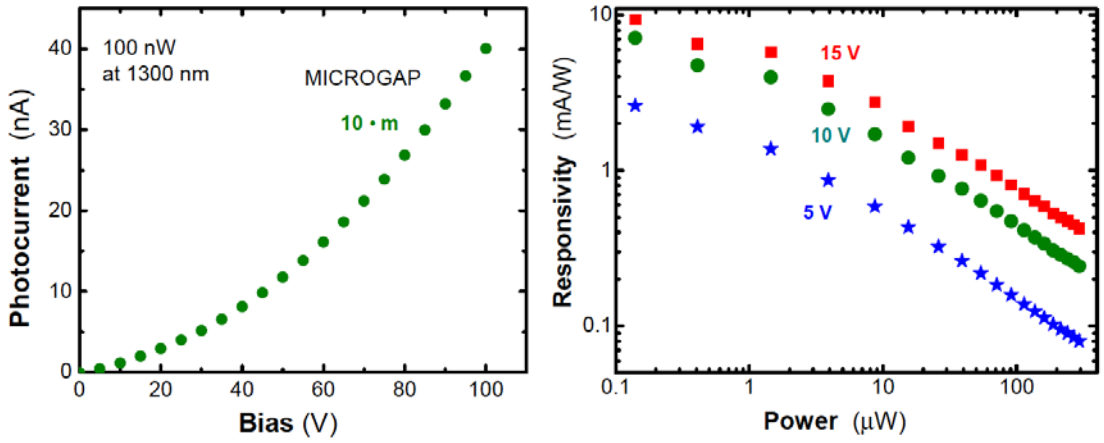

Fig. 25. (a) Photocurrent measured in a single microgap (10 □m gap) photocon illumination at 1300 nm; (b) estimated Responsivity in an interdigitated photoconductor device at several applied bias as a function of the incident power using a 1550 nm laser source (the responsivity is estimated by assuming that all laser light is collected for the device).

Plasmonic effects are expected if the distance between electrodes in a gap-waveguide photoconductor (metal-insulator-metal) is smaller than 100 nm: coupling of light both under normal and in-plane incidence and enhancement of the electric field in the nanogap region. The fabrication of these photoconductor devices (Fig. 26a) on $Si\text{-}SiO_2$ is not simple, because involving several processing steps to define the millimeter size gold pads, micrometer size (from 0.5 to 2 μm) aluminum electrodes and the opened nanogap on them by using RIE after an ebeam patterning on PMMA (Fig. 26b). Still pending the deposition of QDs in the nanogap region that will be made by dispensing the QD ink using a microplotter device and the electro-optical characterization.

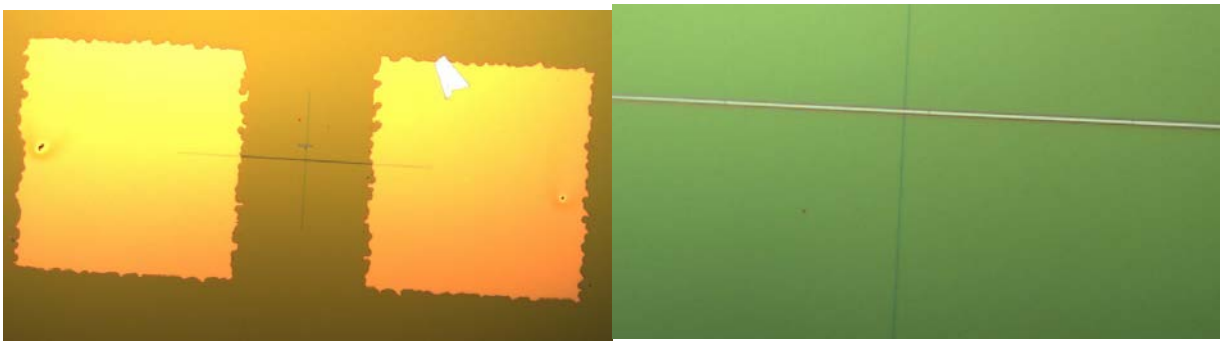

Fig. 26. (a) Nanogap devices fabricated on a Si-SiO_2 substrate, (b) detail of fabrication showing the patterned the nanogap in the PMMA resist prior to RIE.